

Electrical Transport and Grain Growth in Solution-Cast, Chloride-Terminated Cadmium Selenide Nanocrystal Thin Films

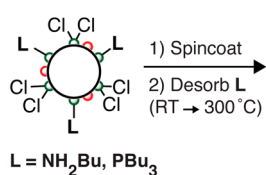
Zachariah M. Norman, Nicholas C. Anderson, and Jonathan S. Owen*

Department of Chemistry, Columbia University, 3000 Broadway, MC 3121, New York, New York 10027, United States

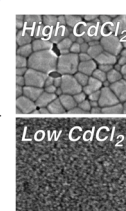
ABSTRACT We report the evolution of electrical transport and grain size during the sintering of thin films spin-cast from soluble phosphine and amine-bound, chloride-terminated cadmium selenide nanocrystals. Sintering of the nanocrystals occurs in three distinct stages as the annealing temperature is increased: (1) reversible desorption of the organic ligands (≤ 150 °C), (2) irreversible particle fusion (200–300 °C), and (3) ripening of the grains to >5 nm domains (>200 °C). Grain growth occurs at 200 °C in films with 8 atom % Cl^- , while films with 3 atom % Cl^- resist growth until 300 °C. Fused

nanocrystalline thin films (grain size = 4.5–5.5 nm) on thermally grown silicon dioxide gate dielectrics produce field-effect transistors with electron mobilities as high as $25 \text{ cm}^2/(\text{Vs})$ and on/off ratios of 10^5 with less than 0.5 V hysteresis in threshold voltage without the addition of indium.

Soluble, Chloride-Terminated CdSe Nanocrystal Ink

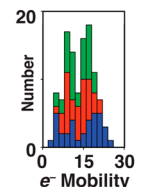


1) Spincoat
2) Desorb L
(RT \rightarrow 300 °C)



FET Mobility

$25 \text{ cm}^2 \text{ V}^{-1} \text{ sec}^{-1}$



KEYWORDS: CdSe quantum dots · nanocrystals · ligand exchange · thin film transistors · stoichiometry · sintering · grazing incidence X-ray scattering · cadmium chloride

Colloidal semiconductor nanocrystals have great potential as inks for printable optoelectronic devices provided that the electrically insulating surfactant shell can be removed.^{1–3} Without organic ligands, the resultant nanocrystals should form close contacts, allowing carriers to delocalize and the charge mobility to increase.^{1,4} Early attempts to achieve this structure replaced the native surfactants on II–VI and IV–VI semiconductor nanocrystals with more volatile and labile organic ligands like pyridine so that films could be cast from solution and the ligand shell desorbed under vacuum. These approaches, however, were unable to completely exchange the starting surfactants^{5,6} and produced films with low charge mobilities ($<1 \text{ cm}^2/(\text{Vs})$) and hysteretic transport.^{7,8}

The difficulty encountered in ligand exchange stems from the cadmium- and lead-rich stoichiometry of these nanocrystals, which balances charge with an anionic surfactant shell.^{9–15} Following Green's covalent bond classification scheme, we refer to these anionic ligands as X-type (e.g., O_2CR ,

HO_3PR , SR , Cl), which are distinct from neutral, two-electron donor ligands, or L-type ligands (e.g., NH_2R , PR_3 , HSR).^{16,17} A third class, Z-type ligands (e.g., $\text{Cd}(\text{O}_2\text{CR})_2$, $\text{Pb}(\text{O}_2\text{CR})_2$, $\text{Cd}(\text{HO}_3\text{PR})_2$, $\text{Zn}(\text{SR})_2$, CdCl_2), acts as neutral *acceptor* ligands that bind the nanocrystals *via* a Lewis acidic interaction with the surface chalcogenide ions.¹⁵ Nanocrystals present a special case for the Green formalism because the surface layer of excess metal ions may or may not be described as part of the ligand shell. The distinction between Z-type ligands and X-type ligands is therefore a semantic one, and a cadmium-rich cadmium selenide nanocrystal with RCO_2^- ligands may equivalently be described as a stoichiometric cadmium selenide nanocrystal with $\text{Cd}(\text{O}_2\text{CR})_2$ ligands.

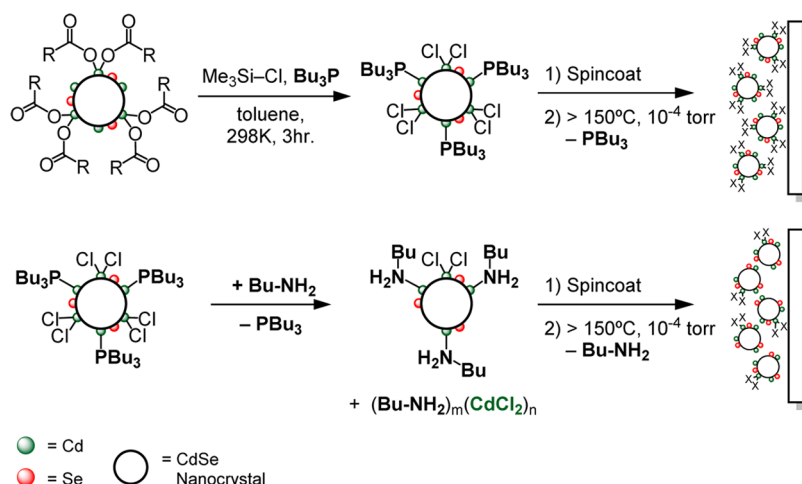
Newer ligand exchange methods that address X-type ligands have led to rapid improvements in the fabrication of high mobility electrical devices. For example, substituting alkylcarboxylate and alkylphosphonate surfactants with metal chalcogenides (such as $[\text{In}_2\text{Se}_4]^{2-}$),¹⁸ S^{2-} ,^{19,20} and $[\text{SCN}]^-$ anions²¹ produces electrostatically stabilized colloids that

* Address correspondence to jso2115@columbia.edu.

Received for review May 23, 2014 and accepted June 24, 2014.

Published online June 24, 2014
10.1021/nn502829s

© 2014 American Chemical Society



Scheme 1. Chloride ligand exchange, film deposition, and thermal desorption of the organic ligand shell.

can be deposited into conductive nanocrystalline films. Thermal annealing at temperatures from 250 to 300 °C in the presence of elemental indium or indium chalcogenides and hydrazine produces solids with electron mobilities in the range of 7–27 cm²/(Vs)^{22,23} that can be used to fabricate integrated circuits on flexible substrates.^{24,25}

While these advances are great strides toward utilizing CdSe nanocrystal solutions to create solution-processed devices, the precise elemental composition of these films and the influence of the annealing step on the electrical transport is not well understood. Further, it is of fundamental interest to study thin films in the absence of foreign metal dopants to determine the intrinsic electrical properties of closely coupled CdSe nanocrystals. There is also little information concerning the mesoscopic structure of conductive films including whether nanocrystals remain isolated but in close contact, fuse into a nanocrystalline network or coalesce into a large grain structure. For example, coalescence of nanocrystals into large grains occurs at 350 °C in CdTe_(2-x)Se_x films in the presence of CdCl₂.²⁶

We recently reported a multigram scale synthesis and detailed characterization of chloride-terminated CdSe nanocrystals bound by *n*-alkylamine (NH₂Bu) and tri-*n*-alkylphosphine (PBu₃) coligands (**CdSe-CdCl₂/L**, L = NH₂Bu, PBu₃).²⁷ Unlike methods which exchange native surfactants for halides in the film state,^{20,28–30} we use well-characterized solutions of **CdSe-CdCl₂/L** to prepare films with precisely defined compositions. Herein we report evidence that NH₂Bu displaces CdCl₂ from the nanocrystal surface and use this effect to tune the coverage of CdCl₂ prior to film deposition and desorption of the organic ligands (Scheme 1). In this way, we assess the influence of the CdCl₂ content on the resultant sintering behavior.

RESULTS AND DISCUSSION

Following our previously reported procedure, chloride-terminated, phosphine-bound cadmium selenide nano-

crystals (**CdSe-CdCl₂/PBu₃**) were prepared by the addition of chlorotrimethylsilane to a solution of PBu₃ (0.5 M) and carboxylate-terminated nanocrystals (**CdSe-Cd(O₂CR)₂**, 2.7–3.4 ⁻O₂CR/nm²) (Scheme 1 and Experimental Methods).^{27,31} The ¹H and ³¹P nuclear magnetic resonance (NMR) spectrum of isolated **CdSe-CdCl₂/PBu₃** shows the expected signals from PBu₃ (0.6 nm⁻², 32 PBu₃ per nanocrystal, *d* = 4 nm) and a minor tri-*n*-butylphosphonium chloride contaminant ([H-PBu₃]⁺[Cl]⁻) (0.02–0.06 nm⁻² 1–3 per nanocrystal, *d* = 4 nm) (Supporting Information Figures S1–S3). The absence of a vinyl resonance from the starting oleyl chain (δ = 5.65 ppm) verifies that the carboxylates are completely removed by reaction with chlorotrimethylsilane.

The PBu₃ ligands (bp = 240 °C) can be exchanged for more volatile primary *n*-alkylamines like *n*-butylamine (NH₂Bu, bp = 78 °C) to assist in the elimination of organics during film annealing (Scheme 1). An amine complex of cadmium chloride [(NH₂Bu)_{*n*}(CdCl₂)_{*m*}] precipitates from the solution 12–36 h after isolation, which was isolated and characterized with FT-IR and energy-dispersive X-ray (EDX) spectroscopies (see Experimental Methods and Figures S4 and S5). These spectroscopic features match those of an independently synthesized *n*-butylamine complex of CdCl₂, which is likely a layered polymeric compound.^{32–34} X-ray photoelectron spectroscopy shows a 62% reduction in the chlorine content caused by the precipitation (Table S1 and Figure S6). These results are consistent with EDX measurements of films prepared from **CdSe-CdCl₂/PBu₃** and **CdSe-CdCl₂/NH₂Bu** where the Cl⁻ content drops from 8 to 3 atom % (Figure S7), corresponding to chloride ligand coverages of 2 and 1 nm⁻², respectively. Thus, much like cadmium carboxylate,¹⁵ CdCl₂ is a labile Z-type ligand and can be displaced by PBu₃ and NH₂Bu as [(PBu₃)_{*n*}(CdCl₂)_{*m*}] and [(NH₂Bu)_{*n*}(CdCl₂)_{*m*}]. Separation of these complexes during the isolation of both **CdSe-CdCl₂/PBu₃** and **CdSe-CdCl₂/NH₂Bu** reduces the X-type ligand coverages compared to the starting **CdSe-Cd(O₂CR)₂**.

With these two nanocrystal samples in hand, we investigated the thermal desorption of their L-type ligands using diffuse reflectance infrared spectroscopy (DRIFTS). Solutions of nanocrystals were slurried with anhydrous potassium bromide and loaded into an *in situ* DRIFTS cell that was evacuated to $<10^{-4}$ Torr and heated while monitoring the vibrational spectrum (Figure 1). This approach allows us to use the absolute signal intensity as a quantitative measure of the relative organic ligand content during desorption. After 2 h under vacuum, the signals from the toluene solvent and free ligands are lost, leaving the signals from PBu_3 and NH_2Bu that are bound to the nanocrystal surface. Higher temperatures drive ligand desorption until 200 °C where 90% of the C–H stretching signal from **CdSe–CdCl₂/PBu₃** disappears. By using the phosphine coverage measured in solution with NMR spectroscopy (32 phosphines/nanocrystal, 0.6 phosphines/nm²), we estimate that 2 ± 1 phosphines per nanocrystal remain (~ 2 atom % carbon) after ligand desorption, an amount on the order of the starting $[\text{HPBu}_3]^+[\text{Cl}]^-$ content. In contrast, $\geq 99\%$ of all signals in the C–H region from **CdSe–CdCl₂/NH₂Bu** are lost by 200 °C, corresponding to less than one amine ligand remaining per nanocrystal (<0.5 atom % carbon). EDX spectroscopy confirmed that nitrogen and phosphorus are eliminated after 2 h of annealing at 250 °C and 10^{-4} Torr.

Annealing the films causes their optical absorption spectra to red shift and broaden as the ligands desorb and the nanocrystals sinter. These changes are gradual below 150 °C and become more dramatic beginning at 200 °C. In the example spectra shown in Figure 1, the first excitonic transitions gradually red shift by 40 meV (**CdSe–CdCl₂/NH₂Bu**) and 20 meV (**CdSe–CdCl₂/PBu₃**) after annealing for 2 h at 150 °C. At the same time, the full width at half-maximum (fwhm) increases by 32 meV (**CdSe–CdCl₂/NH₂Bu**) and 15 meV (**CdSe–CdCl₂/PBu₃**) as the nanocrystals interact more strongly. Surprisingly, these changes can be reversed if the film is exposed to neat primary amines, whereupon it redissolves, recovering the original nanocrystal absorption spectrum (Figure 2). After annealing at 200 °C or higher, the nanocrystals become irreversibly bound within the film and the spectrum broadens and red shifts more dramatically. At 250 °C, the line shape becomes reminiscent of bulk CdSe. We conclude that the small changes to the absorption spectrum occurring below 150 °C reflect a change in inter-nanocrystal separation during ligand loss, while the more dramatic changes that begin near 200 °C result from a distinct structural change that causes much stronger coupling between nanocrystals.

Small- and wide-angle grazing incidence X-ray diffraction (GISAXS and GIWAXS) allow us to directly monitor the mesoscopic structure during sintering.³⁵ GISAXS of unannealed **CdSe–CdCl₂/L** nanocrystal films

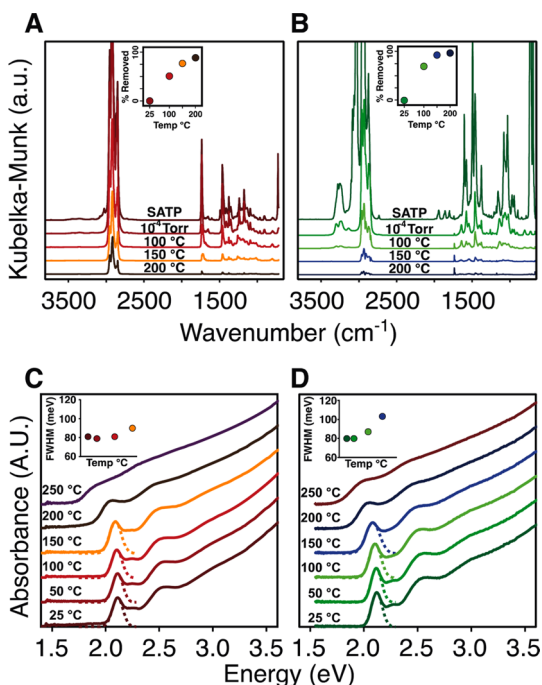


Figure 1. Effect of annealing temperature on the *in situ* diffuse reflectance infrared and UV–visible absorption spectra of **CdSe–CdCl₂/PBu₃** (A,C) and **CdSe–CdCl₂/NH₂Bu** (B,D). Near quantitative amine desorption occurs by 150 °C (B, inset) while $>90\%$ phosphine dissociation occurs by 200 °C (A, inset) (see Experimental Methods for details of quantitative analysis). Changes to the thin film absorption spectrum are nearly identical for both samples, where a significant red shift of the absorption onset and a broadening of the lowest energy transition (inset) occurs above 200 °C.

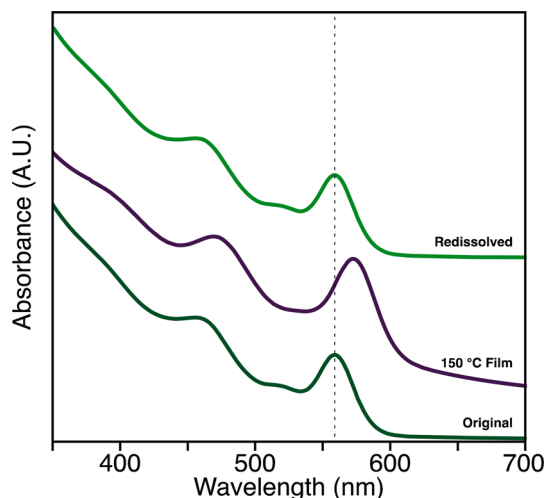


Figure 2. UV–visible spectra, offset for clarity, show a red shift in the first electronic transition after annealing at 150 °C (middle, purple). The film can then be dissolved in a mixture of toluene and *n*-butylamine (top, green), recovering the original optical properties of the particles (bottom, dark green).

produce a pair of isotropic rings at $q = 1.3\text{--}1.4$ and 2.5 nm^{-1} , consistent with a glassy ensemble of quasi-spherical, monodisperse nanocrystals that are 4 nm in diameter and separated by 0.6–0.7 nm of ligand shell (~ 0.7 nm per NH_2Bu or PBu_3 ligand) (Figure 3). Ligands

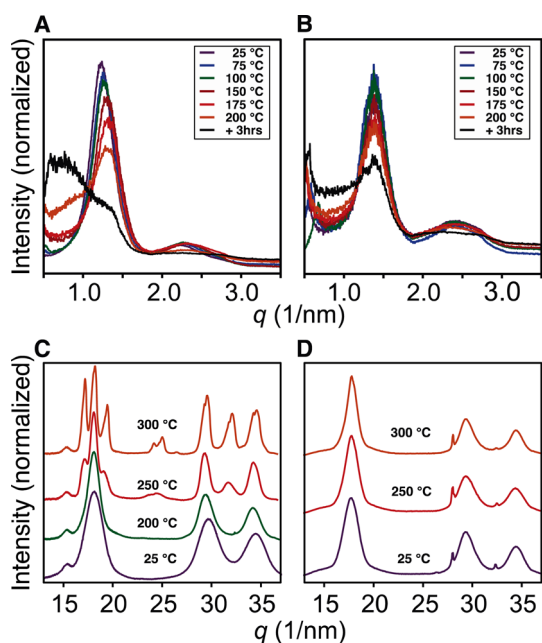


Figure 3. GISAX of CdSe-CdCl₂/PBu₃ (A) and CdSe-CdCl₂/NH₂Bu (B) and GIWAX patterns of CdSe-CdCl₂/PBu₃ (C) and CdSe-CdCl₂/NH₂Bu (D) at several temperatures from 25 to 200 °C. Above 200 °C in (C), reflections from CdCl₂ crystals are visible at 24 and 26 nm⁻¹ ([1,0,4] and [1,0,-5] respectively).

are lost upon annealing under vacuum (10⁻⁴ Torr), reducing the interparticle spacing to near zero, which shifts the inter-nanocrystal scattering correlations to higher q . Above ~ 150 °C, an increase in scattering below $q = 1 \text{ nm}^{-1}$ is observed and the correlations at higher q dissipate, signaling a loss of the regular nanocrystal spacing.³⁵ After 2 h of annealing at 200 °C, the signal from inter-nanocrystal correlations fades, and the pattern resembles diffuse scattering, particularly for films prepared from CdSe-CdCl₂/PBu₃. However, films prepared from CdSe-CdCl₂/NH₂Bu maintain some inter-nanocrystal correlations, suggesting a difference in the sintering kinetics and the resultant mesoscopic structure.

More insight into these differences can be gleaned from the GIWAX patterns, which reveals the crystallite size and phase. In films prepared from CdSe-CdCl₂/NH₂Bu, the broad pattern characteristic of nanometer scale zinc blende crystallites persists up to 300 °C (Figure 3). Scherrer grain size analysis indicates the average grain size increases only slightly after 2 h of annealing at 250 °C ($d = 4 \pm 0.5 \text{ nm}$ to $d = 4.7 \pm 0.5 \text{ nm}$) and an additional 1 nm at 300 °C ($d = 5.7 \pm 0.5 \text{ nm}$). These changes occur simultaneously with the loss of inter-nanocrystal correlations in the GISAXS pattern and may be caused by the oriented attachment of neighboring nanocrystals.³⁶ We interpret these changes as being caused by a sintering process where individual nanocrystals fuse with their nearest neighbors but do not coalesce.

Interestingly, nanocrystal thin films prepared from CdSe-CdCl₂/PBu₃ undergo the same changes at much

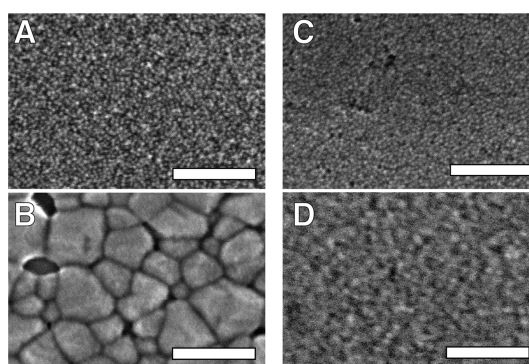


Figure 4. SEM images of CdSe-CdCl₂/PBu₃ films (A) as cast and (B) annealed at 300 °C show clear formation of large wurtzite grains. CdSe-CdCl₂/NH₂Bu films show qualitatively less change (C) before and (D) after annealing at 300 °C. Large void spaces are apparent in B. All scale bars are 100 nm.

lower temperatures (200 °C, $d = 4$ to $5.7 \pm 0.5 \text{ nm}$). At temperatures above 200 °C, a phase transition to wurtzite occurs and the diffraction lines narrow. The now broad distribution of large grains can be analyzed with scanning electron microscopy (SEM) and transmission electron microscopy (TEM) of slices prepared by focused ion beam sectioning (Figure 4 and Figure S8). Smooth, crack-free films of individual nanocrystals are replaced by contiguous, large crystal domains ($\leq 100 \text{ nm}$) in films annealed at 300 °C. A significant density of voids between nanocrystals and between the nanocrystals and the substrate is clearly visible in the SEM images and TEM cross sections (Figures S8–S10). Thus, a clear difference in the extent of ripening was observed depending on the starting nanocrystal composition. Films prepared from CdSe-CdCl₂/PBu₃ begin to form larger grain sizes at temperatures as low as 200 °C and rapidly reach tens of nanometer length scales at 250 °C (Figure S12), while ripening in the films prepared from CdSe-CdCl₂/NH₂Bu is much slower, and the original nanocrystal size and crystal phase are maintained until 300 °C or higher.

A series of control experiments demonstrate that the change in growth kinetics is caused by the CdCl₂ concentration rather than the amine or phosphine ligands. For example, the grain size remains unaffected if PBu₃ is added to the solution used to spin-coat CdSe-CdCl₂/NH₂Bu or if nanocrystalline thin films derived from sintering CdSe-CdCl₂/NH₂Bu were dipped in PBu₃ and subsequently reannealed under vacuum. However, if a sintered nanocrystal film prepared from CdSe-CdCl₂/NH₂Bu at 200 °C is dipped in a methanol or anhydrous tetrahydrofuran solution saturated with CdCl₂, a large grain wurtzite structure forms after annealing at 200 °C. This is consistent with previous reports on II–VI semiconductor thin films prepared by close-space sublimation, electrochemical deposition, solution-processed nanocrystals, or spray pyrolysis, where it was shown that grain growth is catalyzed by CdCl₂.^{26,37–42} Thus, a relatively small

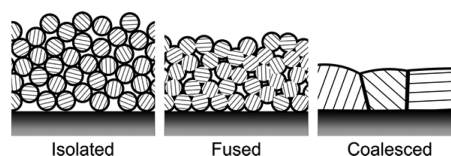
change in the chemical composition of the nanocrystal films can greatly influence the sintering process.

Interestingly, near the temperature where grain growth ensues, micrometer scale CdCl_2 crystals form that are visible in SEM images as well as in the GIWAXS patterns (Figures 3 and S12). The coincidence of the CdCl_2 crystallite formation and the onset of CdSe grain growth suggests that the diffusion of CdCl_2 near 200 °C is linked to the diffusion of CdSe. This is perhaps a consequence of the Lewis acidity of CdCl_2 , which can bind selenide anions and increase their mobility. Indeed, ripening of colloidal CdSe nanocrystals is known to be catalyzed by acids.⁴³ In the 8 atom % Cl^- , the CdSe diffusion is rapid and the grains grow more easily, while in films with 3 atom % Cl^- , the CdSe diffusion is relatively slow and <5 nm grains are maintained at 250 °C and below. However, slow CdSe diffusion across the grain boundary may help grow the intergrain contact area, irreversibly fusing the nanocrystals to one another and causing the red-shifting and broadening of the UV–vis despite the apparent lack of grain growth in the GIWAXS.

Collectively, these observations support a three-phase annealing process as the temperature increases: (1) ligands desorb between room temperature and 150 °C, producing films of isolated nanocrystalline grains; (2) the film sinters as nanocrystals irreversibly fuse with their nearest neighbors yet maintain their original size (150–250 °C); (3) the nanocrystals begin to coalesce into larger grains (200–350 °C) (Scheme 2). The temperature at which each of these transitions occurs depends on the ligand type, including both the L-type donors and the coverage of Z-type CdCl_2 . In particular, small changes to the CdCl_2 content have a significant influence on the mesoscale structure. This clearly highlights the importance of reproducible control over the nanocrystal composition and the ligand exchange.

Having demonstrated that the grain size can be tuned by altering the nanocrystal composition, we sought to correlate the mesostructure with the electrical transport properties. Thin film transistors (TFTs) were prepared by spin-casting and thermally annealing 30–100 nm CdSe nanocrystals on silicon wafers with 200 nm thermal oxide and then evaporating aluminum top contacts (100 μm channel lengths, $W/L = 30$). N-type conductivity becomes significant ($>10^{-4}$ S/cm) in films annealed to 200 °C or above, a temperature where irreversible sintering begins and the more dramatic broadening and red-shifting of the absorption spectra is observed. The transconductance was negligible below 200 °C.

Across 5 thin films (15 devices, 6 traces per device) prepared from three separate syntheses of **CdSe- $\text{CdCl}_2/\text{NH}_2\text{Bu}$** annealed at 250 °C and with <5 nm domains, an average field-effect mobility was extracted in the linear region ($\langle\mu_{\text{lin}}\rangle = 14(5)$ $\text{cm}^2/(\text{Vs})$) (Figure 5E). Low hysteresis in the threshold voltage ($\pm 1V_{\text{th}}$), a subthreshold slope of 4 V/decade, and the



Scheme 2. Three stages of nanocrystal sintering during thermal annealing.

high on/off ratio of 10^5 are all indicative of a high-quality semiconductor film free from mobile ions (Figure 5A). Additionally, the 3 V median threshold voltage (V_{th}) and carrier concentration of $3 \times 10^{16} \text{ cm}^{-3}$ are similar to other CdSe nanocrystal films on silicon dioxide^{22,23} and suggestive of a relatively low density of unfilled trap states.

Surprisingly, the larger grain wurtzite films prepared from **CdSe- $\text{CdCl}_2/\text{PBU}_3$** showed poorer transistor characteristics with lower median electron mobilities of $\langle\mu_{\text{lin}}\rangle = 1.3 \text{ cm}^2/(\text{Vs})$ (Figure 5C). Larger off currents and large and negative threshold voltages (-8 V) stem from a more heavily doped material ($2.0 \times 10^{17} \text{ cm}^{-3}$). These films also have larger subthreshold slopes, 60 V/decade versus 4 V/decade for the nanocrystalline films above, which suggests a more defective electronic structure. Thus, despite the larger grain size observed in the GIWAXS and SEM images, the electrical transport is mediated by a greater concentration of defects with lower average mobility. This defective structure may be caused by the voids that separate nanocrystals from one another and from the substrate or by the high concentration of dopants. For example, previous studies of II–VI semiconductors have shown that selenium vacancies^{44–46} and chloride dopants^{47,48} give rise to an increased carrier concentration and defect density. In the present study, these structures may form because of the relatively high chloride content (3–8 atom %, Figure S7). Additionally, the reaction of PBU_3 ligands with selenium during the annealing process or poor wetting of the silicon dioxide substrate during grain growth could contribute to the transport properties observed.

The observed electrical characteristics correlate well with the three phase sintering model described in Scheme 2 and illustrate the importance of the fusion process to the electron mobility. Most importantly, desorbing the PBU_3 or NH_2Bu ligands and allowing the nanocrystals to intimately interact does not lead to substantial conductivity. This is perhaps surprising considering the 15–30 meV broadening of the lowest energy excitonic absorption feature, evidence of carrier delocalization. Instead, the films remain resistive ($>1 \times 10^7 \Omega\text{cm}$) and do not exhibit a gate effect unless the sample is heated to irreversibly fuse the grains, at which point more substantial broadening of the absorption spectrum occurs.

The nanocrystalline films prepared in this work are comparable to polycrystalline thin films of CdSe formed by evaporation and electrodeposition.^{44,49–52} These films

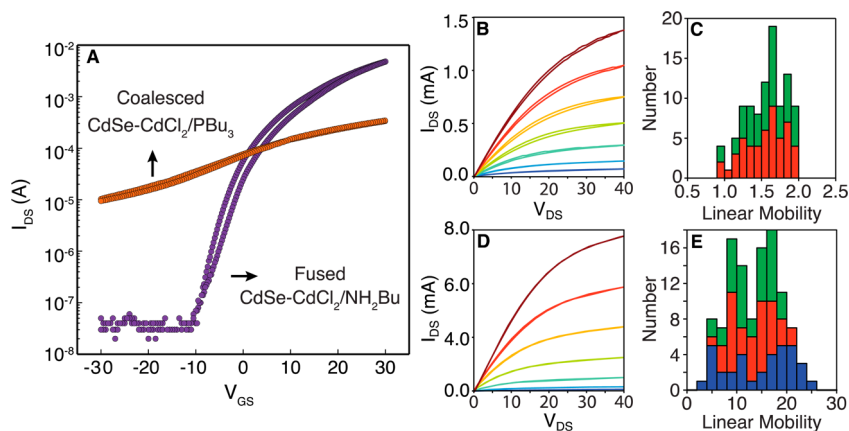


Figure 5. (A) Transfer characteristics representative of CdSe-CdCl₂/PBu₃ and CdSe-CdCl₂/NH₂Bu TFTs are shown on the left. The CdSe-CdCl₂/PBu₃ transfer characteristics display a negative threshold voltage (~ 8 V) and low on/off ratio (~ 100), while the CdSe-CdCl₂/NH₂Bu transfer characteristics turn on at positive gate bias (3 V) and have a large on/off ratio (10^5). Each scan was acquired over 10–20 s. Output characteristics for CdSe-CdCl₂/PBu₃ (B) and CdSe-CdCl₂/NH₂Bu (D) TFTs with V_{GS} increasing from -10 (dark blue) to 50 V (dark red) in 10 V steps. (Bottom, middle column) shows a reduction in current at $V_{GS} = 0$ as well as a reduction in hysteresis. The right column displays a histogram of linear mobilities extracted from the transfer characteristics for CdSe-CdCl₂/PBu₃ (C) and CdSe-CdCl₂/NH₂Bu (E), respectively. Each color represents a separate nanocrystal synthesis that was examined across 3–6 different devices and demonstrates the reproducibility of this method.

have electron mobilities ranging from 3 to $100 \text{ cm}^2/(\text{Vs})$ and carrier concentrations ranging from 10^{11} to 10^{18} cm^{-3} , which are sensitive to the grain size, annealing temperature, and are enhanced by doping with indium.^{47,53,54} In these studies, the grain size in the high-performance materials approaches 100 nm ; however, our work clearly demonstrates that strong electronic coupling between nanocrystalline grains ($<5 \text{ nm}$) can reliably produce films with comparably high carrier mobilities ($10\text{--}20 \text{ cm}^2/(\text{Vs})$) and low carrier concentrations (10^{16} cm^{-3}).

Nanocrystal solids with compact inorganic ligands are often discussed as superlattices in which the individual nanocrystals couple to form new bands of electronic states where the interparticle coupling strength and the degree of site disorder determines the final mode of transport.^{4,8,22,55,56} Our work provides clear evidence that desorption of the organic ligand shell is insufficient to achieve the coupling required for high charge mobilities and indicates that subsequent fusion of the nanocrystal solid is necessary. Previous studies of conductive CdSe nanocrystal solids annealed samples above 200°C to achieve electron mobilities above $1 \text{ cm}^2/(\text{Vs})$, implying that fusion and grain growth may also play a role in those studies. Moreover, the chemical composition of the nanocrystalline film sensitively influences the kinetics of the sintering process. In this study, a relatively small amount of Lewis acidic CdCl₂ was important to the

final mesostructure, but other acidic impurities can also be expected to cause grain growth,⁴³ while others might prevent fusion or contribute hysteretic currents. The chemical composition is precisely controlled in the present study, allowing us to prepare films that display consistent sintering and transport characteristics.

CONCLUSION

We demonstrated that high mobility field-effect transistors can be fabricated from soluble nanocrystals following exchange of their carboxylate ligands for chloride. TFT performance on par with state of the art nanocrystal thin films was obtained without optimizing the gate dielectric or doping with indium. The mesostructure of the resulting film depends sensitively on the annealing temperature and time, as well as the presence of CdCl₂, a variable that we control using solution ligand exchange methods. The sensitivity of the sintering process to the presence of CdCl₂ clearly illustrates how small changes in the nanocrystal composition can influence the mesostructure and transport. Thus, detailed studies of electrical transport require reproducible and tunable nanocrystal surface chemistry. Moreover, we observed that charge mobilities greater than $0.1 \text{ cm}^2/(\text{Vs})$ required fusion of the nanocrystal solid and was not achieved upon ligand desorption alone. This conclusion helps explain why high annealing temperatures are broadly utilized to obtain high mobility devices from colloidal CdSe nanocrystals.

EXPERIMENTAL METHODS

General Considerations. Cadmium nitrate tetrahydrate (99%), sodium hydroxide, myristic acid (99%), selenium dioxide (99.8%), anhydrous oleic acid (99%), and 1-octadecene (90%)

were purchased from Sigma-Aldrich and used as received. Benzene-*d*₆ (99.6%) and anhydrous methyl acetate (99.5%) were purchased from Sigma-Aldrich, shaken with activated alumina, filtered, and stored over 4 \AA molecular sieves at least

24 h prior to use. Pentane and toluene were dried using a solvent purification column, shaken with fresh activated alumina, and stored over 4 Å molecular sieves at least 24 h prior to use. Tri-*n*-butylphosphine (99%) was purchased from Strem and used without further purification in a nitrogen glovebox. Chlorotrimethylsilane (99%) and *n*-butylamine (99%) were purchased from Sigma-Aldrich, dried over CaH₂, distilled, and stored in a sealed Strauss flask under argon. Highly p-doped, 1–20 Ωcm, [100] silicon wafers with 200 nm of dry thermal oxide were purchased from Silicon Quest International.

All manipulations were performed under air-free conditions unless otherwise indicated using standard Schlenk techniques or within a nitrogen-filled glovebox. Cadmium tetradecanoate was synthesized from cadmium nitrate and myristic acid on 22 mmol scale following previously reported procedures.^{27,31} NMR spectra were recorded on Bruker Avance III 400 and 500 MHz instruments. ¹H NMR spectra were acquired with sufficient relaxation delay to allow complete relaxation between pulses (>30 s). ³¹P NMR spectra were recorded with 2 s delays between pulses. UV–visible absorption spectra were obtained using a PerkinElmer Lambda 950 spectrophotometer equipped with deuterium and tungsten halogen lamps, 150 mm integrating sphere with an InGaAs/PMT detector. Scanning electron microscopy was performed using a Hitachi 4700 tungsten cold field emission scanning electron microscope. Electrode deposition was performed using an Angstrom Amod deposition system installed in a nitrogen glovebox. Electrical measurements were performed in a nitrogen glovebox using an Agilent 4155C semiconductor parameter analyzer.

Synthesis and Isolation of CdSe-Cd(O₂CR)₂. Zinc blende CdSe nanocrystals were synthesized using a previously reported method.^{27,31} In a typical synthesis, a 2 L flask is charged with 12.76 g of cadmium tetradecanoate, 2.5 g of selenium dioxide, and 1.5 L of octadecene, degassed, and heated to 240 °C. Volatile organics were then removed by vacuum distillation (130–135 °C, 20–50 mbar), and the residue was transferred to a nitrogen glovebox for purification via precipitation from pentane with methyl acetate. After isolation, a stock solution was prepared in benzene-*d*₆ and ¹H NMR and UV–visible absorption spectroscopies were used to estimate the surface ligand density as described previously.²⁷

Synthesis of CdSe-CdCl₂/PBu₃ and CdSe-CdCl₂/NH₂Bu. CdSe-CdCl₂/PBu₃ was prepared following previously reported methods.²⁷ In brief, to a toluene solution of nanocrystals ([[−]O₂CR] = 0.083 M) and Bu₃P (0.5 M), Me₃Si–Cl was added (12 equiv/[−]O₂CR ligand) and the solution stirred for 3 h. The volatile component was removed by vacuum distillation, and the solid was purified via precipitation from toluene with pentane. Amine exchange was accomplished by dissolving a known volume of CdSe-CdCl₂/PBu₃ stock solution in neat *n*-butylamine. Pentane was then added and purification by precipitation was performed. When the freshly exchanged nanocrystals are stored in solution with *n*-butylamine for 24 h, a white amine complex of CdCl₂ forms (Figures S5 and S6 and Table S1), which may be removed by filtration. The purified nanocrystals were stored in solutions of toluene and *n*-butylamine (10 vol %).

DRIFTS Analysis. 60 μL of CdSe nanocrystal stock solution (0.2 mM in nanocrystals) was mixed with KBr (0.5 g, <8 wt %) and ground in a mortar and pestle inside a nitrogen glovebox. The mixture was loaded into the high-temperature stage of a Thermo Nicolet 6700 FTIR with Praying Mantis attachment. The chamber was sealed under partial vacuum (>600 Torr) and placed within the beam path of the DRIFTS cell. The chamber was then connected to another vacuum pump fitted with an LN₂ cold trap and evacuated to <10^{−4} Torr. KBr blanks were taken in an identical manner for each temperature, and all data were processed by algorithmic baseline correction followed by the Kubelka–Munk transformation so that spectral intensity was proportional to concentration.

EDS Analysis. Energy-dispersive spectroscopy was performed using a Hitachi 4700 cold field emission SEM equipped with a Si(Li) detector. Samples were prepared on either Si wafers coated in 30 nm Au with a 5 nm Cr adhesion layer or on highly

ordered pyrolytic graphite freshly exfoliated with transparent tape. An electron energy of 20 keV was used for excitation, and the Se Kα, Cd Lα, and Cl Kα lines were analyzed using the Spirit software package.

Film Formation and Annealing. Silicon wafers were diced into 2.5 cm squares, washed with isopropyl alcohol, sonicated in isopropyl alcohol for 15 min, and dried under flowing nitrogen and then in an oven at 160 °C for 15 min before being brought into a nitrogen drybox. Substrates were then washed at 1700 rpm for 45 s with 3 mL of dry toluene passed through a 0.2 μm filter immediately prior to spin-casting.

A 200 μL nanocrystal solution, 0.2 mM in nanocrystals (~25 mg/mL), was dropped onto the substrates and allowed to wet the entire surface. The substrate was spun at 600–1700 rpm to form a film 50–100 nm in thickness, which displays a strong specular reflection and color that changes as a function of the angle from which it is viewed. These are features of Fresnel reflection from a smooth interface.

Substrates were transferred to a tube furnace under flowing argon, which was then immediately evacuated to 10^{−5} Torr. The tube furnace was then heated to 200 °C and held for 30 min, at which point argon was reintroduced and allowed to flow at 15 sccm over the samples. The temperature was then increased to the desired value and held for 2 h under flowing argon and allowed to slowly cool to room temperature. The tube furnace was then opened under flowing argon, and the samples were immediately transferred to a nitrogen drybox.

X-ray Diffraction Experiments. X-ray diffraction experiments were performed using the X9 beamline at the National Synchrotron Light Source (NSLS) at Brookhaven National Laboratory or using the D1 line at the Cornell High Energy Synchrotron Source (CHESS). All synchrotron diffraction experiments were performed on 1 cm × 1 cm samples prepared identically to thin film transistors or on 1 cm × 1 cm sections cut from transistor devices. Diffraction patterns were taken at incident angles of 0.07–0.30°, aligning the sample immediately prior to the measurement. Beam exposure time ranged from 3 to 10 s, empirically chosen to avoid saturating the detector. Measurements at CHESS were performed under ambient conditions, while all measurements at NSLS were performed at 10^{−3} Torr. *In situ* annealing was performed at NSLS using a heated stage. The detector positions were determined using a silver behenate standard. A 2D detector analysis was performed using a combination of Fit2d, View.gtk, and pyXSanalysis software suites.

Cross Sectional Transmission Electron Microscopy. Transmission electron micrograph cross sections from annealed nanocrystal films were prepared by focused ion beam lithography at Brookhaven National Lab. Micrographs were taken using a JEOL JEM2100F at the Center for Functional Nanomaterials at Brookhaven National Lab with a 200 keV accelerating voltage with the beam normal to the section plane.

Thin Film UV–Visible Spectroscopy. Nanocrystal films were cast on glass slides and annealed at temperatures ranging from 25 to 250 °C for 2 h at 10^{−4} Torr. Transmission and reflection spectra were taken using an integrating sphere equipped with an InGaAs detector. The $-\log(t/t_0 + r/r_0)$ was plotted against wavelength and normalized at 350 nm, where *t* is the transmitted signal, *t*₀ is the transmission through an identical glass slide, *r* is the reflected signal, and *r*₀ is the 100% reflection baseline calibrated to Spectralon.

Transistor Fabrication. Deposition of aluminum electrodes was performed using a shadowmask in an Ångström Engineering deposition system. SEM was used to measure the channel length after deposition (60–100 μm range), the value of which was used to model of the electrical data. The channel width was 3 mm. Typical device dimensions were 50–75 nm of CdSe nanocrystals on highly p-doped Si wafers with 200 nm of dry thermal oxide dielectric and 100 nm thick Al electrodes.

Modeling. Transfer curves were modeled using nonlinear least-squares fitting to ideal MOSFET models. Modeling was performed using the Enthought Python Distribution with the Python Data Analysis Library (pandas), Numeric Python (NumPy), Science Python (SciPy), and Matplotlib. The drain current was modeled in the saturation (*V*_{DS} > *V*_{GS} − *V*_t) and

linear regimes ($V_{DS} < V_{GS} - V_t$):

$$I_{d,sat} = \frac{W}{2L} \mu C_{ox} (V_{GS} - V_t)^2$$

$$I_{d,lin} = \frac{W}{L} \mu V_{DS} C_{ox} \left(V_{GS} - V_t - \frac{V_{DS}}{2} \right)$$

where W , L , C_{ox} , μ , V_t , V_{GS} , and V_{DS} are the channel width, channel length, oxide capacitance, field-effect mobility, threshold voltage, gate-source bias, and drain-source bias, respectively. The W and L were measured using SEM after each measurement, while C_{ox} was computed from the thickness and dielectric constant of the oxide. Only μ and V_t parameters were extracted from the fit. Nonlinear least-squares fitting was performed for both transfer and output characteristics, and similar results were obtained. We define hysteresis as the absolute value of the difference between threshold voltage when reversing a transfer sweep.

Conductivity was extracted from the $V_{GS} = 0$ output characteristics by taking the slope about $V_{DS} = 0$, assuming that the current passes through a volume with dimension $W \times L \times$ thickness as measured by SEM and assuming that the contact resistance was much less than the channel resistance. The carrier concentration was computed by dividing the conductivity by the elementary charge and $\langle \mu \rangle$.

Conflict of Interest: The authors declare the following competing financial interest(s): The corresponding author is a paid consultant at Pacific Light Technologies, which utilizes semiconductor nanoparticles in commercial applications.

Acknowledgment. This research was supported by the Department of Energy under Grant No. DE-SC0006410. N.C.A. was supported by the National Science Foundation Research Fellowship under Grant No. DGE07-07425. Use of the National Synchrotron Light Source, Brookhaven National Laboratory, was supported by the U.S. Department of Energy, Office of Basic Energy Sciences under Contract No. DE-AC02-98CH10886. Research conducted at the Cornell High Energy Synchrotron Source (CHESS) is supported by the National Science Foundation and the National Institutes of Health/National Institute of General Medical Sciences under NSF Award DMR-0936384. We thank K. Kisslinger for preparing film cross section for TEM analysis. We also thank D. Smilgies at CHESS, K. Yager and L. Yang at Brookhaven National Laboratory, and A. Wolcott, all of whom assisted with grazing incidence X-ray diffraction experiments. We also acknowledge J. Choi, whose constant motivation and many insightful conversations informed much of this work, as well as O. Yaffe, who added much clarity to the presentation of this work. Additionally, I. Kymissis provided important insight into the electrical measurements.

Supporting Information Available: Figures describing supporting X-ray, FTIR, NMR, elemental and electron microscopy analyses are available in the Supporting Information. This material is available free of charge via the Internet at <http://pubs.acs.org>.

REFERENCES AND NOTES

- Talpin, D. V.; Lee, J.-S.; Kovalenko, M. V.; Shevchenko, E. V. Prospects of Colloidal Nanocrystals for Electronic and Optoelectronic Applications. *Chem. Rev.* **2010**, *110*, 389–458.
- Mitzi, D.; Kosbar, L.; Murray, C.; Copel, M.; Afzali, A. High-Mobility Ultrathin Semiconducting Films Prepared by Spin Coating. *Nature* **2004**, *428*, 299–303.
- Street, R. A. Thin-Film Transistors. *Adv. Mater.* **2009**, *21*, 2007–2022.
- Shabaev, A.; Efros, A. L.; Efros, A. L. Dark and Photo-Conductivity in Ordered Array of Nanocrystals. *Nano Lett.* **2013**, *13*, 5454–5461.
- Katari, J. E.; Colvin, L. V.; Alivisatos, A. P. X-ray Photoelectron Spectroscopy of CdSe Nanocrystals with Applications to Studies of the Nanocrystal Surface. *J. Phys. Chem.* **1994**, *98*, 4109–4117.
- Kuno, M.; Lee, J. K.; Dabbousi, B. O.; Mikulec, F. V.; Bawendi, M. G. The Band Edge Luminescence of Surface Modified CdSe Nanocrystallites: Probing the Luminescing State. *J. Chem. Phys.* **1997**, *106*, 9869.
- Ridley, B. A.; Nivi, B.; Jacobson, J. M. All-Inorganic Field Effect Transistors Fabricated by Printing. *Science* **1999**, *286*, 746–749.
- Ginger, D. S.; Greenham, N. C. Charge Injection and Transport in Films of CdSe Nanocrystals. *J. Appl. Phys.* **2000**, *87*, 1361.
- Moreels, I.; Fritzing, B.; Martins, J. C.; Hens, Z. Surface Chemistry of Colloidal PbSe Nanocrystals. *J. Am. Chem. Soc.* **2008**, *130*, 15081–15086.
- Owen, J. S.; Park, J.; Trudeau, P.-E.; Alivisatos, A. P. Reaction Chemistry and Ligand Exchange at Cadmium–Selenide Nanocrystal Surfaces. *J. Am. Chem. Soc.* **2008**, *130*, 12279–12281.
- Taylor, J.; Kippeny, T.; Rosenthal, S. J. Surface Stoichiometry of CdSe Nanocrystals Determined by Rutherford Backscattering. *J. Cluster Sci.* **2001**, *12*, 571–582.
- Fritzing, B.; Capek, R. K.; Lambert, K.; Martins, J. C.; Hens, Z. Utilizing Self-Exchange To Address the Binding of Carboxylic Acid Ligands to CdSe Quantum Dots. *J. Am. Chem. Soc.* **2010**, *132*, 10195–10201.
- Morris-Cohen, A. J.; Frederick, M. T.; Lilly, G. D.; McArthur, E. A.; Weiss, E. A. Organic Surfactant-Controlled Composition of the Surfaces of CdSe Quantum Dots. *J. Phys. Chem. Lett.* **2010**, *1*, 1078–1081.
- Luther, J. M.; Pietryga, J. M. Stoichiometry Control in Quantum Dots: A Viable Analog to Impurity Doping of Bulk Materials. *ACS Nano* **2013**, *7*, 1845–1849.
- Anderson, N. C.; Hendricks, M. P.; Choi, J. J.; Owen, J. S. Ligand Exchange and the Stoichiometry of Metal Chalcogenide Nanocrystals: Spectroscopic Observation of Facile Metal-Carboxylate Displacement and Binding. *J. Am. Chem. Soc.* **2013**, *135*, 18536–18548.
- Green, M. L. H.; Parkin, G. Application of the Covalent Bond Classification Method for the Teaching of Inorganic Chemistry. *J. Chem. Educ.* **2014**, *91*, 807–816.
- Green, M. L. H. A New Approach to the Formal Classification of Covalent Compounds of the Elements. *J. Organomet. Chem.* **1995**, *500*, 127–148.
- Kovalenko, M.; Scheele, M.; Talpin, D.; Kovalenko, M.; Scheele, M.; Talpin, D. Colloidal Nanocrystals with Molecular Metal Chalcogenide Surface Ligands. *Science* **2009**, *324*, 1417–1420.
- Liu, Y.; Tolentino, J.; Gibbs, M.; Ihly, R.; Perkins, C. L.; Liu, Y.; Crawford, N.; Hemminger, J. C.; Law, M. PbSe Quantum Dot Field-Effect Transistors with Air-Stable Electron Mobilities above $7 \text{ cm}^2 \text{ V}^{-1} \text{ s}^{-1}$. *Nano Lett.* **2013**, *13*, 1578–1587.
- Zhang, H.; Hu, B.; Sun, L.; Hovden, R.; Wise, F. W.; Muller, D. A.; Robinson, R. D. Surfactant Ligand Removal and Rational Fabrication of Inorganically Connected Quantum Dots. *Nano Lett.* **2011**, *11*, 5356–5361.
- Fafarman, A. T.; Koh, W.; Diroll, B. T.; Kim, D. K.; Ko, D.-K.; Oh, S. J.; Ye, X.; Doan-Nguyen, V.; Crump, M. R.; Reifsnnyder, D. C.; et al. Thiocyanate-Capped Nanocrystal Colloids: Vibrational Reporter of Surface Chemistry and Solution-Based Route to Enhanced Coupling in Nanocrystal Solids. *J. Am. Chem. Soc.* **2011**, *133*, 15753–15761.
- Choi, J.-H.; Fafarman, A. T.; Oh, S. J.; Ko, D.-K.; Kim, D. K.; Diroll, B. T.; Muramoto, S.; Gillen, J. G.; Murray, C. B.; Kagan, C. R. Bandlike Transport in Strongly Coupled and Doped Quantum Dot Solids: A Route to High-Performance Thin-Film Electronics. *Nano Lett.* **2012**, *12*, 2631–2638.
- Lee, J.-S.; Kovalenko, M.; Huang, J.; Chung, D.; Talpin, D. Band-like Transport, High Electron Mobility and High Photoconductivity in All-Inorganic Nanocrystal Arrays. *Nat. Nanotechnol.* **2011**, *6*, 348–352.
- Kim, D. K.; Lai, Y.; Diroll, B. T.; Murray, C. B.; Kagan, C. R. Flexible and Low-Voltage Integrated Circuits Constructed from High-Performance Nanocrystal Transistors. *Nat. Commun.* **2012**, *3*, 1216.
- Chung, D. S.; Lee, J.-S.; Huang, J.; Nag, A.; Ithurria, S.; Talpin, D. V. Low Voltage, Hysteresis Free, and High

- Mobility Transistors from All-Inorganic Colloidal Nanocrystals. *Nano Lett.* **2012**, *12*, 1813–1820.
26. MacDonald, B. I.; Martucci, A.; Rubanov, S.; Watkins, S. E.; Mulvaney, P.; Jasieniak, J. J. Layer-by-Layer Assembly of Sintered CdSe_{1-x}Te_x Nanocrystal Solar Cells. *ACS Nano* **2012**, *6*, 5995–6004.
 27. Anderson, N. C.; Owen, J. S. Soluble, Chloride-Terminated CdSe Nanocrystals: Ligand Exchange Monitored by ¹H and ³¹P NMR Spectroscopy. *Chem. Mater.* **2013**, *25*, 69–76.
 28. Tang, J.; Kemp, K. W.; Hoogland, S.; Jeong, K. S.; Liu, H.; Levina, L.; Furukawa, M.; Wang, X.; Debnath, R.; Cha, D.; et al. Colloidal-Quantum-Dot Photovoltaics Using Atomic-Ligand Passivation. *Nat. Mater.* **2011**, *10*, 765–771.
 29. Voznyy, O.; Zhitomirsky, D.; Stadler, P.; Ning, Z.; Hoogland, S.; Sargent, E. H. A Charge-Orbital Balance Picture of Doping in Colloidal Quantum Dot Solids. *ACS Nano* **2012**, *6*, 8448–8455.
 30. Ning, Z.; Ren, Y.; Hoogland, S.; Voznyy, O.; Levina, L.; Stadler, P.; Lan, X.; Zhitomirsky, D.; Sargent, E. H. All-Inorganic Colloidal Quantum Dot Photovoltaics Employing Solution-Phase Halide Passivation. *Adv. Mater.* **2012**, *24*, 6295–6299.
 31. Chen, O.; Chen, X.; Yang, Y.; Lynch, J.; Wu, H.; Zhuang, J.; Cao, Y. C. Synthesis of Metal-Selenide Nanocrystals Using Selenium Dioxide as the Selenium Precursor. *Angew. Chem., Int. Ed.* **2008**, *47*, 8638–8641.
 32. Evans, R.; Mann, F.; Peiser, H.; Purdie, D. The Constitution of Complex Metallic Salts. Part XI. The Structure of the Tertiary Phosphine and Arsine Derivatives of Cadmium and Mercuric Halides. *J. Chem. Soc.* **1940**, 1209.
 33. Bernard, M. A.; Busnot, F.; Le Querler, J. F. Halogenures de Zinc, Cadmium et Mercure (II) Solvates Par Des Amines Aliphatiques. Conclusions Sur La Stabilité Thermique et L'étude Thermochimique Des Ces Composés. *Thermo-chim. Acta* **1979**, *33*, 249–257.
 34. Dakternieks, D. Phosphorus-31 and Cadmium-113 N.M.R. Studies of Cadmium(II) Complexes with Some Tertiary Phosphines. *Aust. J. Chem.* **1982**, *35*, 469.
 35. *X-ray and Neutron Reflectivity. Principles and Applications*, 1st ed.; Daillant, J. Gibaud, A., Eds.; Springer: Berlin, 2009.
 36. Smilgies, D.-M. Scherrer Grain-Size Analysis Adapted to Grazing-Incidence Scattering with Area Detectors. *J. Appl. Crystallogr.* **2009**, *42*, 1030–1034.
 37. McCandless, B.; Dobson, K. Processing Options for CdTe Thin Film Solar Cells. *Sol. Energy* **2004**, *77*, 839–856.
 38. Barrioz, V.; Irvine, S.; Jones, E.; Rowlands, R.; Lamb, D. *In Situ* Deposition of Cadmium Chloride Films Using MOCVD for CdTe Solar Cells. *Thin Solid Films* **2007**, *515*, 5808–5813.
 39. Krishna, K. V.; Dutta, V. Effect of *In Situ* CdCl₂ Treatment on Spray Deposited CdTe/CdS Heterostructure. *J. Appl. Phys.* **2004**, *96*, 3962.
 40. Loginov, Y.; Durose, K.; Al-Allak, H.; Galloway, S.; Oktik, S.; Brinkman, A.; Richter, H.; Bonnet, D. Transmission Electron Microscopy of CdTe/CdS Based Solar Cells. *J. Cryst. Growth* **1996**, *161*, 159–163.
 41. Bayhan, H.; Erçelebi, C. Electrical Characterization of Vacuum-Deposited N-CdS/p-CdTe Heterojunction Devices. *Semicond. Sci. Technol.* **1997**, *12*, 600–608.
 42. Townsend, T. K.; Yoon, W.; Foos, E. E.; Tischler, J. G. Impact of Nanocrystal Spray Deposition on Inorganic Solar Cells. *ACS Appl. Mater. Interfaces* **2014**, *6*, 7902–7909.
 43. Owen, J. S.; Chan, E. M.; Liu, H.; Alivisatos, A. P. Precursor Conversion Kinetics and the Nucleation of Cadmium Selenide Nanocrystals. *J. Am. Chem. Soc.* **2010**, *132*, 18206–18213.
 44. Wynands, H.; Cocivera, M. Hall Effect and Resistivity Characterization of Doped, Electrodeposited CdSe. *J. Electrochem. Soc.* **1992**, *139*, 2052.
 45. Tubota, H.; Suzuki, H.; Hirakawa, K. On the Mechanism of the Electrical Conduction in CdSe. *J. Phys. Soc. Jpn.* **1960**, *15*, 1701.
 46. Szabo, J. P.; Cocivera, M. Effect of Annealing Atmosphere on the Properties of Thin-Film CdSe. *J. Appl. Phys.* **1987**, *61*, 4820.
 47. Chaudhuri, S.; Bhattacharyya, J.; De, D.; Pal, A. K. Characterization of CdS Film Prepared by Hot Wall Technique. *Sol. Energy Mater.* **1984**, *10*, 223–233.
 48. Chaudhuri, S.; Dhar, A.; Pal, A. K. Studies of Some Wide Band Gap II–VI Semiconductor Based p-n Junctions. *Vacuum* **1990**, *41*, 853–855.
 49. Chan, D. S. H.; Hill, A. E. Conduction Mechanisms in Thin Vacuum-Deposited Cadmium Selenide Films. *Thin Solid Films* **1976**, *35*, 337–349.
 50. Brodie, D. E.; Yeh, G. Hall Studies on Encapsulated CdSe Films. *Can. J. Phys.* **1968**, *46*, 1993–2000.
 51. Vanfleteren, J.; van Calster, A. A Four-Vacuum-Cycle Lift-off Process for the Polycrystalline CdSe Thin-Film Transistor. *IEEE Electron Device Lett.* **1985**, *6*, 11–13.
 52. Erskine, J. C. Cadmium Selenide Thin-Film Transistors. *J. Vac. Sci. Technol.* **1978**, *15*, 1823.
 53. Eisenmann, B.; Schäfer, H. Cd-In-Se, Ternary Phase Diagram. In Landolt-Börnstein Database, <http://www.springer-materials.com/docs/index.html>; pp 83–160.
 54. Van Calster, A.; Vervaet, A.; de Rycke, I.; de Baets, J.; Vanfleteren, J. Polycrystalline CdSe Films for Thin Film Transistors. *J. Cryst. Growth* **1990**, *86*, 924–928.
 55. Guyot-Sionnest, P. Electrical Transport in Colloidal Quantum Dot Films. *J. Phys. Chem. Lett.* **2012**, *3*, 1169–1175.
 56. Liu, H.; Pourret, A.; Guyot-Sionnest, P. Mott and Efros-Shklovskii Variable Range Hopping in CdSe Quantum Dots Films. *ACS Nano* **2010**, *4*, 5211–5216.